

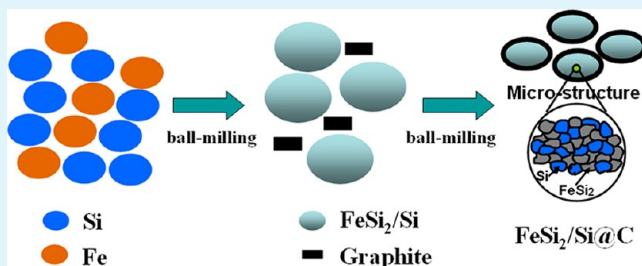
# Green Synthesis and Stable Li-Storage Performance of $\text{FeSi}_2/\text{Si}@\text{C}$ Nanocomposite for Lithium-Ion Batteries

Yao Chen, Jiangfeng Qian, Yuliang Cao, Hanxi Yang, and Xinping Ai\*

Hubei Key Laboratory of Electrochemical Power Sources, College of Chemistry & Molecule Science, Wuhan University, Wuhan, 430072, China

**ABSTRACT:** Si-based alloy materials have received great attention as an alternative anode for high capacity and safe Li-ion batteries, but practical implementation of these materials is hindered by their poor electrochemical utilization and cyclability. To tackle this problem, we developed a core–shelled  $\text{FeSi}_2/\text{Si}@\text{C}$  nanocomposite by a direct ball-milling of Fe and Si powders. Such a nanostructured composite can effectively buffer the volumetric change by alloying active Si phase with inactive  $\text{FeSi}_2$  matrix in its inner cores and prevent the aggregation of the active Si particles by outer graphite shells, so as to improve the cycling stability of the composite material. As a result, the  $\text{FeSi}_2/\text{Si}@\text{C}$  composite exhibits a high Li-storage capacity of  $\sim 1010 \text{ mA g}^{-1}$  and an excellent cyclability with 94% capacity retention after 200 cycles, showing a great promise for battery applications. More significantly, the synthetic method developed in this work possesses several advantages of low cost, zero emission, and operational simplicity, possibly to be extended for making other Li-storage alloys for large-scale applications in Li-ion batteries.

**KEYWORDS:** lithium ion battery, ball milling, Si anode,  $\text{FeSi}_2/\text{Si}$  alloy, core–shell structure,  $\text{FeSi}_2/\text{Si}@\text{C}$  Nanocomposite



## INTRODUCTION

Developing a new generation of lithium ion batteries (LIB) with substantially improved energy density and safety is an urgent demand for a number of new energy technology applications ranging from portable electronics to electrical vehicles and to renewable energy storages.<sup>1,2</sup> A critical issue for this technology development is to find safer and higher capacity anodes to substitute the graphite anodes used in current LIB technology, which have only a theoretical capacity of  $372 \text{ mA h g}^{-1}$  and a low working potential nearby lithium deposition potential. In this technological pursuit, various lithium-storable metals and alloys have been widely explored in the past decades,<sup>3–7</sup> and among them, silicon has attracted particular attention because of its highest Li-storage capacity of  $4200 \text{ mA h g}^{-1}$  ( $\text{Li}_{4.4}\text{Si}$ ) and moderate thermodynamic lithiation potential ( $+0.2 \text{ V}$ , Vs Li).<sup>8</sup> However, the commercial application of Si anodes is still seriously hindered by their poor cyclability resulted from the huge volumetric changes ( $>300\%$ ) during lithium insertion/extraction cycles, leading to a severe pulverization and deactivation of the active particles.<sup>9</sup>

To alleviate the volume change at charge–discharge cycling, researchers have adopted various strategies to buffer the mechanical stress of lithiated Si anodes by use of nanosized Si particles,<sup>10–17</sup> ultrathin film electrodes,<sup>18–20</sup> Si alloy nanocomposites,<sup>21–23</sup> and porous Si nanostructures.<sup>24,25</sup> Although some of the nanoarchitected Si particles can achieve considerably high capacity and cyclability,<sup>18,20,25–29</sup> they are usually obtained through complicated chemical

synthetic procedures, which are difficult to extend for large-scale battery applications.

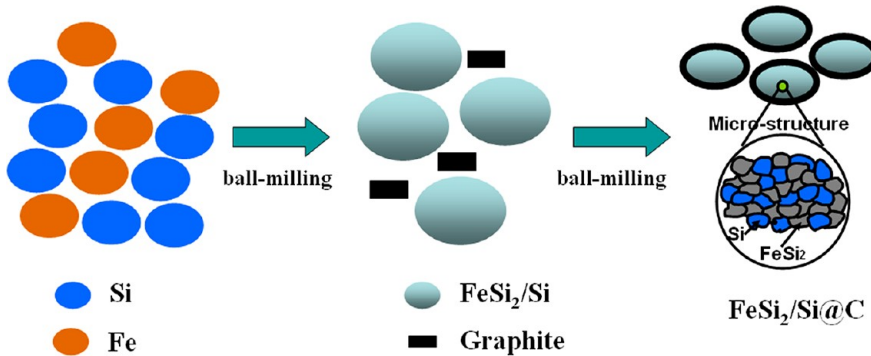
Our previous works have revealed that some of commercially available and low-cost Si alloys can also serve as high capacity Li-storage anodic host materials with certain cyclability.<sup>30,31</sup> If such Si alloy compounds can be made with required chemical stoichiometry and structural architecture through a simple mechanochemical process, it would bring about a great flexibility for developing Li-storage anodic materials with respect to conventional high temperature metallurgy and a remarkable decrease in materials cost and pollutant emission with regard to the currently used sol–gel synthesis, thus ensuring sustainable Li-ion battery applications.

Here, we describe a core–shelled  $\text{FeSi}_2/\text{Si}@\text{C}$  nanocomposite by direct high-energy milling a stoichiometric ratio of Si and Fe powders to form  $\text{FeSi}_2/\text{Si}$  alloy composite and then carbon-coating the  $\text{FeSi}_2/\text{Si}$  composite by further planetary milling alloy with graphite to produce the core–shell nanoparticles. Such a biphasic core consists of a buffering  $\text{FeSi}_2$  phase forming on the surface of active Si particles during the mechanochemical reaction of Fe and Si, which allows reversible Li alloying with and buffers the volume expansion of the Si lattices. The graphite-coated outer shells act as both a conductive network and an additional confining buffer layer, providing enhanced electron conduction and a strong

Received: May 28, 2012

Accepted: July 3, 2012

Published: July 3, 2012

Scheme 1. Schematic Illustration for Preparing  $\text{FeSi}_2/\text{Si}@\text{C}$  Composites

restriction for the volume change of the inner active Si cores during Li alloying and dealloying cycling. As expected, the  $\text{FeSi}_2/\text{Si}@\text{C}$  nanocomposite thus prepared can not only deliver a high reversible Li-storage capacity of  $\sim 1010 \text{ mA h g}^{-1}$  but also demonstrate an excellent cycling stability with almost indiscernible capacity fading over 200 cycles. More significantly, the synthetic method developed in this work possesses several advantages of low-cost, zero emission, and operational simplicity, possibly to be extended for making other Li-storage alloys for large-scale applications in Li-ion batteries.

## EXPERIMENTAL SECTION

**Materials Preparation and Characterizations.** The  $\text{FeSi}_2/\text{Si}@\text{C}$  composite was prepared by a two-step ball-milling process. First, a 3:1 weight ratio of commercial Si (Alfa Aesar, 325 mesh) and Fe powder (Alfa Aesar, 325 mesh) was mixed and ball-milled in a SPEX-8000 high-energy mechanical mill for 10 h. Then, the reactant product was further ball milled with graphite powder (99% purity,  $< 5 \mu\text{m}$ ) in a planetary mill (QM-1SP04, Nanjing, China) with the rotation speed of 200 rpm for 6 h. The weight ratio of graphite to the total amount of Si + Fe was designed as 1:9, so that the final composite contains 67.5 wt % Si, 22.5 wt % Fe, and 10 wt % graphite. The weight ratio of milling balls to the powder materials in the planetary milling process was 20:1. All the milling processes were performed under Ar atmosphere.

The crystalline structures and surface morphologies of the as-prepared powder examples were characterized by X-ray diffraction (XRD, Shimadzu XRD-6000) using  $\text{Cu K}\alpha$  radiation, scanning electron microscopy (SEM, Quanta 200, FEI, Netherlands), and transmission electron microscopy (TEM, JEOL, JEM-2010-FEF).

**Electrochemical Measurements.** To evaluate the electrochemical properties, we prepared the  $\text{FeSi}_2/\text{Si}@\text{C}$  composite anode by casting the electrode slurry onto a  $20 \mu\text{m}$  thick copper foil. The electrode slurry consisted of 70 wt % active material, 10 wt % acetylene black and 20 wt % poly(acrylic acid) (PAA) as a binder, dissolved in distilled water. The electrode was dried at  $80^\circ\text{C}$  under a vacuum for overnight to remove the water and then roll-pressed to obtain a dense anode-active layer of  $0.02 \text{ mm}$  thick. The PAA binder used in this study has an average molecule weight of 240 000, purchased from Alfa Aesar.

The charge-discharge experiments were performed using CR2016-type coin cells with Celgard 2400 microporous membrane as separator and a lithium disk as counter electrode. The electrolyte was 1 M  $\text{LiPF}_6$  dissolved in a mixture of ethylene carbonate (EC), dimethyl carbonate (DMC) and ethyl methyl carbonate (EMC) (1:1:1 in volume ratio, Shinestar Battery Materials Co., Ltd., China). The cells were assembled in an argon-filled glovebox with oxygen and water contents less than 10 ppm. The electrochemical performances were evaluated on a Land Battery Testing System (Wuhan Kingnuo Electronics Co., Ltd., China) at  $25^\circ\text{C}$ . The cutoff voltage is 0.005 V versus  $\text{Li}/\text{Li}^+$  for discharge (Li insertion) and 1.5 V versus  $\text{Li}/\text{Li}^+$  for charge (Li extraction). The specific capacity was calculated on the mass weight of the anode-active nanocomposite. Cyclic voltammetry (CV) were

carried out on an electrochemical workstation (CHI660a, Shanghai, China) in a voltage range of 0.005 V–1.5 V at a scan rate of  $0.1 \text{ mV s}^{-1}$ .

## RESULTS AND DISCUSSION

The mechanochemical formation of the  $\text{FeSi}_2/\text{Si}@\text{C}$  nanocomposite is schematically illustrated in Scheme 1. Elemental Fe and Si powers were selected as starting raw materials because of their commercial availability and stoichiometric convenience. At first step, the Fe and Si powers reacted to form a biphasic  $\text{FeSi}_2/\text{Si}$  composite with a buffering  $\text{FeSi}_2$  phase grown on the surface of Si cores at vigorous collisions during high-energy ball milling. After that, the resulting  $\text{FeSi}_2/\text{Si}$  particles were further surface-coated with graphite to give  $\text{FeSi}_2/\text{Si}@\text{C}$  nanocomposite particles at planetary ball-milling.

The formation reactions of the  $\text{FeSi}_2/\text{Si}@\text{C}$  composite can be evidenced from the changes of the XRD signals of the Fe–Si system in the duration of ball-milling, as shown in Figure 1.

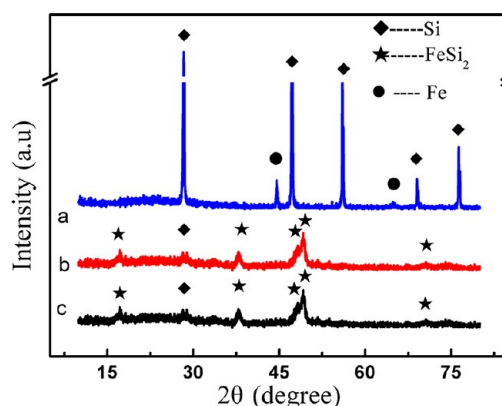


**Figure 1.** XRD patterns of the Fe–Si system: (a) Fe and Si mixture before ball-milling, (b) Fe–Si alloy after ball-milling, and (c) Fe–Si–graphite composite after further ball-milling Fe–Si alloy with graphite.

Before milling, the XRD pattern of the Fe–Si system shows sharp peaks of Si and Fe, demonstrating their presence both in elemental states. After being milled, the diffraction peaks of Si became much weaker and broader, implying a great decrease in its size and crystallinity. Meanwhile, the XRD signals of Fe diminished with increased milling time and disappeared finally and instead, a number of new diffractions emerged at  $2\theta = 17.2^\circ$ ,  $37.6^\circ$ ,  $47.7^\circ$ , and  $48.9^\circ$ , reflecting a complete conversion of Fe into the  $\text{FeSi}_2$  phase at the ball milling condition. Since Fe is much ductile than Si, the resulting  $\text{FeSi}_2$  phase should be anchored on the surfaces of the Si cores. As designed with a

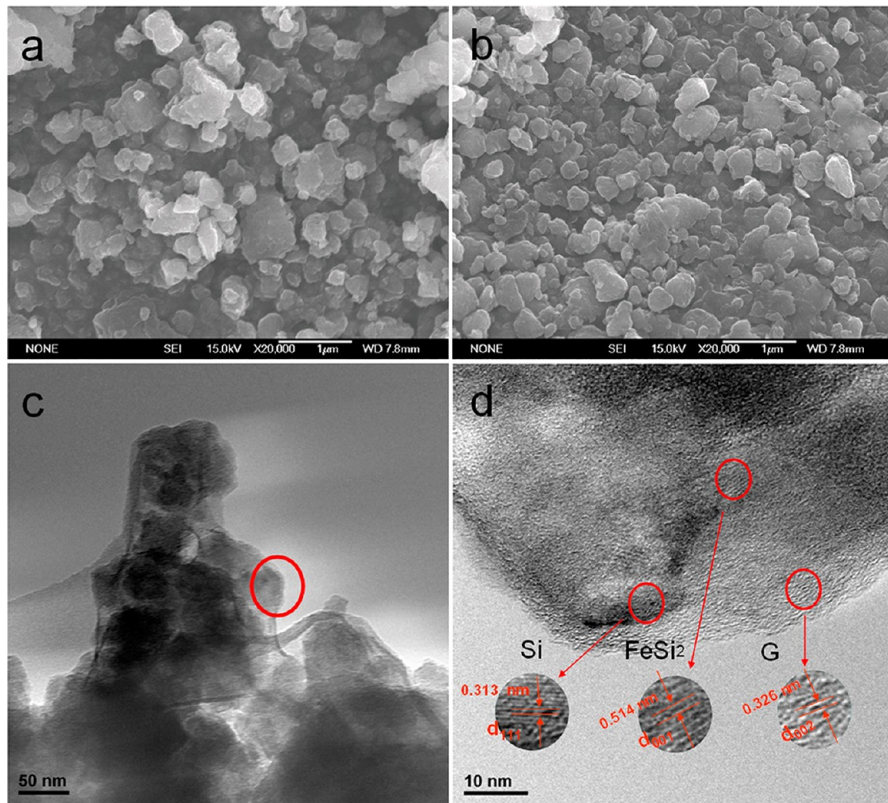


**Figure 2.** (a) SEM image of Si/FeSi<sub>2</sub> alloy particles. (b–d) SEM image, TEM image and HR-TEM image of Si/FeSi<sub>2</sub>/graphite composite, respectively. The insets in d are the magnified images of the regions marked by the red circle.

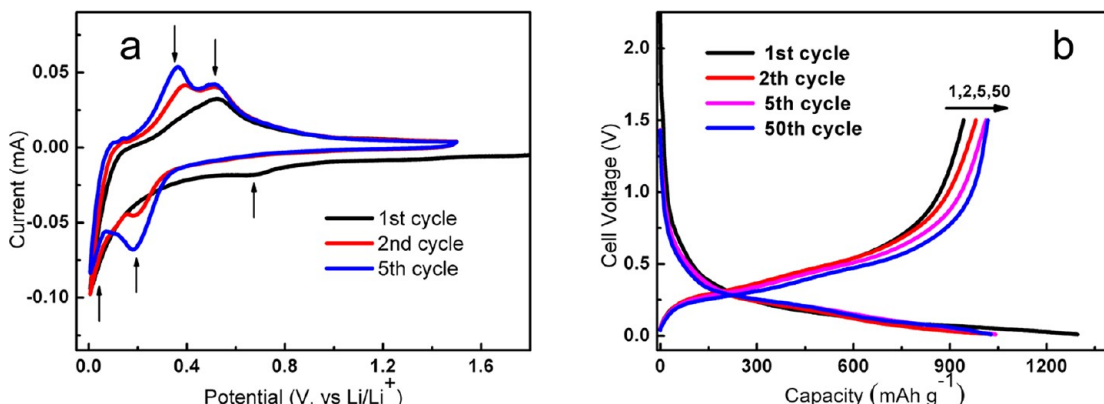


**Figure 3.** (a) CV curves of the FeSi<sub>2</sub>/Si@C composite electrode in 1 M LiPF<sub>6</sub>/EC–DMC–EMC electrolyte and (b) galvanostatic discharge–charge curves for different cycles.

starting mass ratio of Si:Fe = 3:1, the final contents of the active Si and inactive FeSi<sub>2</sub> in the FeSi<sub>2</sub>/Si@C nanocomposite should be close to 1:1, i.e., the alloy composition could be expressed as FeSi<sub>2</sub>/4Si. When the FeSi<sub>2</sub>/Si alloy was further milled with graphite, there were no any new phases appeared in the XRD pattern of the FeSi<sub>2</sub>/Si@C particles and the typical (002) peak of the graphite at 26.4° was not detected (Figure 1c), indicating that the FeSi<sub>2</sub>/Si cores maintained unchanged and that the layered graphite structure was smashed during the planetary milling.

The structural and morphological features of the FeSi<sub>2</sub>/Si@C particles can be seen from its SEM and TEM images given in Figure 2. As displayed in the figures, the FeSi<sub>2</sub>/Si powers appear as irregular particles with their size at 200–500 nm and

remain almost the same size and morphology even coated by graphite. The magnified TEM image (Figure 2c) reveals that each particle of the FeSi<sub>2</sub>/Si@C composite is composed of smaller crystallites of ~50 nm, which were produced and welded together during the mechanochemical cold fracturing/welding reactions. The core–shelled structure of the nanocomposite can be visualized from the cross-sectional TEM image of a single particle. As seen from the locally magnified image of the edge of a particle (Figure 2d), there is a 5–8 nm thick outer layer with the lattice fringes of 0.326 nm, corresponding to the *d* spacing values of the (002) plane of hexagonal graphite. Since the outer graphite layer is only several nanometers thick and appears as defected fringes, the failure to detect its presence in the FeSi<sub>2</sub>/Si@C composite from XRD

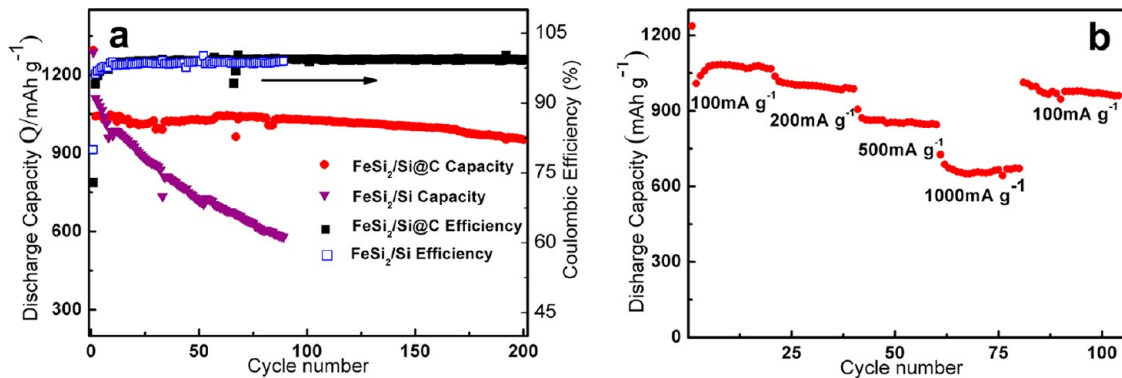


**Figure 4.** (a) Cycling performance of the FeSi<sub>2</sub>/Si@C composite and FeSi<sub>2</sub>/Si alloy electrode. (b) Rate capability of the FeSi<sub>2</sub>/Si@C composite electrode.

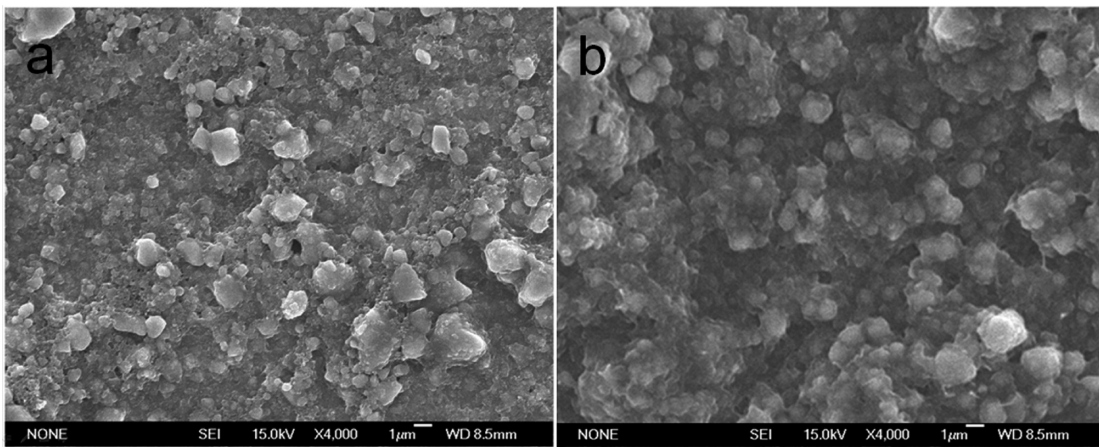


**Figure 5.** SEM images of FeSi<sub>2</sub>/Si@C composite electrode (a) before and (b) after 20 cycles.

analysis is understandable. Also, two kinds of lattice fringes with basal distances of 0.313 and 0.513 nm can be observed from the inner parts of the image, which reflect the (111) plane of cubic silicon (JCPDS #27-1402) and the (001) plane of tetragonal FeSi<sub>2</sub> (JCPDS #35-0822), respectively.

To identify the electrochemical Li-alloying reactions on this composite, we measured cyclic voltammograms (CV) of the FeSi<sub>2</sub>/Si@C electrode in the low potential region from 1.5 to 0.005 V at a scan rate of 0.1 mV s<sup>-1</sup>. As shown in Figure 3a, the composite electrode displays a constant cathodic current in the first negative scan starting from 1.5 to 0.3 V, due to the irreversible reduction of electrolyte solvent for the formation of solid electrolyte interphase (SEI) film on the composite anode. When the potential scan proceeds, a sharp cathodic peak arises at a low potential of 0.2 V and a broad anodic band appears correspondingly with its peak current at 0.5 V on the reversed scan, which are characteristic of the reversible Li alloying/dealloying reactions with active Si phase in the composite. Since the second scan and thereafter, two pairs of reversible redox peaks appear constantly in the CV curves with their cathodic/anodic peaks centered at 0.08/0.39 V and 0.16/0.51 V respectively, showing two-stage alloying reactions of Li<sup>+</sup> on the Si phase with the formation of two different lithiated states of Li<sub>x</sub>Si. These CV features are in good agreement with the well-documented CV data of the Si-based electrodes.<sup>4,32</sup>

Figure 3b displays the discharge-charge profiles of the FeSi<sub>2</sub>/Si@C composite electrode at a current density of 100 mA g<sup>-1</sup>, measured from 2032 coin type Li-FeSi<sub>2</sub>/Si@C cells. In

the first cycle, the FeSi<sub>2</sub>/Si@C electrode delivered initial charge/discharge (lithium alloying/dealloying) capacities of 1296/942 mAh g<sup>-1</sup>, corresponding to an initial Coulombic efficiency of 72%. As is well-known, there always exists an irreversible capacity loss due to the electrochemical reduction of electrolyte for the formation of SEI film and the partial deactivation of inserted lithium in the host lattice, particularly in the case of Si-alloy anodes.<sup>33-35</sup> Because the second cycle, the charge/discharge efficiency of the electrode rose rapidly up to  $\geq 92\%$  and arrived at  $\geq 99\%$  after a few cycles, meanwhile the reversible lithium storage capacity increased from its initial 942 mA h g<sup>-1</sup> to a stable 1010 mA h g<sup>-1</sup> at fifth cycle, showing a typical activation process. This activation process is frequently encountered in the Si-based electrodes using poly(acrylic acid) (PAA) as a binder and is usually attributed to the strong adherence of PAA binder on the Si surface and the poor absorption ability of PAA for electrolyte, which lead to a slow soaking of electrolyte in the inner area of the electrode and therefore give rise to a gradual activation of the electrode-active material.<sup>36</sup>

Figure 4a compares the cycling capacities and the Coulombic efficiencies of the FeSi<sub>2</sub>/Si@C composite and FeSi<sub>2</sub>/Si alloy electrodes at a constant current of 100 mA g<sup>-1</sup>. Although the FeSi<sub>2</sub>/Si alloy anode exhibited a slightly high reversible capacity of  $\sim 1287$  mAh g<sup>-1</sup> and a relatively high Coulombic efficiency of  $\sim 80\%$  in the initial cycle, its capacity decreased rapidly down to  $< 600$  mAh g<sup>-1</sup> after 90 cycles, showing a very low capacity retention of  $\sim 45\%$ . In contrast, the FeSi<sub>2</sub>/Si@C composite

electrode demonstrated a strong cycleability with a reversible capacity of  $\sim 940 \text{ mA h g}^{-1}$  at 200th cycle, corresponding to superior capacity retention of  $\sim 93\%$  with respect to its highest capacity at fifth cycle. At the same time, the Coulombic efficiency kept stably at 99% at prolonged cycles. This comparison suggests a determining role of the graphite coating in enhancing the cycling stability of the alloy electrode. In the light of its structural features, the excellent cyclability of the  $\text{FeSi}_2/\text{Si}@\text{C}$  composite could be accounted for by two reasons: (1) the inert  $\text{FeSi}_2$  phase in the alloy core can effectively alleviate the volume expansions of active Si; (2) the outer graphite layer acts as a ductile buffer to further accommodate the mechanical stress and also maintain good electrical contact of the electroactive particles during repeated cycles.

The rate capability of the  $\text{FeSi}_2/\text{Si}@\text{C}$  composite electrode is given in Figure 4b. When the current density was increased successively from  $100 \text{ mA g}^{-1}$  to  $200 \text{ mA g}^{-1}$  and further to  $500 \text{ mA g}^{-1}$ , the capacity declined slightly from  $1010 \text{ mA h g}^{-1}$  to  $\sim 990 \text{ mA h g}^{-1}$  and  $\sim 880 \text{ mA h g}^{-1}$ . Even at a very high current of  $1000 \text{ mA g}^{-1}$ , the composite anode can still deliver a reversible capacity of  $>700 \text{ mA h g}^{-1}$ , showing a good rate capability. Once the current density was returned to  $100 \text{ mA g}^{-1}$ , the reversible capacity of  $\sim 950 \text{ mA g}^{-1}$  can be recovered. Apparently, the good rate capability of the  $\text{FeSi}_2/\text{Si}@\text{C}$  composite benefits from the graphite-coating layer that provides not only greatly improved electrical conductivity but also sufficient  $\text{Li}^+$  transport tunnels.

The morphological changes of the  $\text{FeSi}_2/\text{Si}@\text{C}$  composite electrode before and after 20 cycles were investigated by SEM (Figure 5). To avoid the surface contamination from environments, the surface layer of the Si/ $\text{FeSi}_2$ /graphite composite electrode was scraped off before SEM measurements. Compared to the uncycled electrode, the SEM image of the electrode after 20 cycles did not show any distinguishable change in morphology. This structural and morphological stability is no doubt a main cause for the cycling stability of the  $\text{FeSi}_2/\text{Si}@\text{C}$  composite.

## CONCLUSIONS

In summary, we have successfully prepared a core–shelled  $\text{FeSi}_2/\text{Si}@\text{C}$  composite by a simple ball milling process. This composite is composed of an outer layer of graphite and an inner Si/ $\text{FeSi}_2$  core formed by mechanochemical reaction of Fe and Si powders. The as-prepared  $\text{FeSi}_2/\text{Si}@\text{C}$  composite shows not only a highly stable reversible capacity of  $\sim 1010 \text{ mA h g}^{-1}$  with  $\sim 94\%$  capacity retention after 200 cycles, but also a good rate capability with  $>700 \text{ mAh g}^{-1}$  at current density of  $1000 \text{ mA g}^{-1}$  when used as anode materials for rechargeable lithium batteries. In addition, the synthetic route developed in this work is very simple, low-cost, and pollution-free, enabling it to be adopted for large-scale production and also to be extended for making other Li-storage alloy materials with improved capacity utilization and cycling stability.

## AUTHOR INFORMATION

### Corresponding Author

\*E-mail: xpai@whu.edu.cn. Phone: +86-27-68754526.

### Notes

The authors declare no competing financial interest.

## ACKNOWLEDGMENTS

We thank the 973 Program (2009CB2 20100) of China, the National 863 Program of China (2011AA11A254), the Fundamental Research Funds for the Central University and the National Science Foundation of China (21173160).

## REFERENCES

- (1) Armand, M.; Tarascon, J. M. *Nature* **2008**, *451*, 652–657.
- (2) Kulova, T. L.; Skundin, A. M. *Russ. J. Electrochem.* **2012**, *48*, 330–335.
- (3) Huggins, R. A. *J. Power Sources* **1999**, *81–82*, 13–19.
- (4) Boukamp, B. A.; Lesh, G. C.; Huggins, R. A. *J. Electrochem. Soc.* **1981**, *128*, 725–729.
- (5) Zhou, Y. N.; Wang, X. J.; Lee, H. S.; Nam, K. W.; Yang, X. Q.; Haas, O. *J. Appl. Electrochem.* **2011**, *41*, 271–275.
- (6) Park, C.-M.; Kim, J.-H.; Kim, H.; Sohn, H.-J. *Chem. Soc. Rev.* **2010**, *39*, 3115–3141.
- (7) Chou, C. Y.; Kim, H.; Hwang, G. S. *J. Phys. Chem. C* **2011**, *115*, 20018–20026.
- (8) Wei-Jun, Z. *J. Power Sources* **2011**, *196*, 13–24.
- (9) Ryu, J. H.; Kim, J. W.; Sung, Y.-E.; Oh, S. M. *Electrochem. Solid-State Lett.* **2004**, *7*, A306–A309.
- (10) Munao, D.; Valvo, M.; Van Erven, J.; Kelder, E. M.; Hassoun, J.; Panero, S. *J. Mater. Chem.* **2012**, *22*, 1556–1561.
- (11) Iwamura, S.; Nishihara, H.; Kyotani, T. *J. Phys. Chem. C* **2012**, *116*, 6004–6011.
- (12) Hieu, N. S.; Lim, J. C.; Lee, J. K. *Microelectron. Eng.* **2012**, *89*, 138–140.
- (13) Yao, Y.; McDowell, M. T.; Ryu, I.; Wu, H.; Liu, N. A.; Hu, L. B.; Nix, W. D.; Cui, Y. *Nano Lett.* **2011**, *11*, 2949–2954.
- (14) Chan, C. K.; Peng, H.; Liu, G.; Mcilwrath, K.; Zhang, X. F.; Huggins, R. A.; Cui, Y. *Nat. Nanotechnol.* **2008**, *3*, 31–35.
- (15) Kim, H.; Seo, M.; Park, M. H.; Cho, J. *Angew. Chem., Int. Ed.* **2010**, *49*, 2146–2149.
- (16) Shin, K.; Park, D.-J.; Lim, H.-S.; Sun, Y.-K.; Suh, K.-D. *Electrochim. Acta* **2011**, *58*, 578–582.
- (17) Choi, H. S.; Lee, J. G.; Lee, H. Y.; Kim, S. W.; Park, C. R. *Electrochim. Acta* **2010**, *56*, 790–796.
- (18) Cui, L. F.; Hu, L. B.; Choi, J. W.; Cui, Y. *ACS Nano* **2010**, *4*, 3671–3678.
- (19) Yu, C. J.; Li, X.; Ma, T.; Rong, J. P.; Zhang, R. J.; Shaffer, J.; An, Y. H.; Liu, Q.; Wei, B. Q.; Jiang, H. Q. *Adv. Energy Mater.* **2012**, *2*, 68–73.
- (20) Choi, J. A.; Kim, D. W.; Bae, Y. S.; Song, S. W.; Hong, S. H.; Lee, S. M. *Electrochim. Acta* **2011**, *56*, 9818–9823.
- (21) Santos-Pena, J.; Brousse, T.; Schleich, D. M. *Ionics* **2000**, *6*, 133–138.
- (22) Lee, H.-Y.; Lee, S.-M. *J. Power Sources* **2002**, *112*, 649–654.
- (23) Cakan, R. D.; Titirici, M. M.; Antonietti, M.; Cui, G. L.; Maier, J.; Hu, Y. S. *Chem. Commun.* **2008**, 3759–3761.
- (24) Chen, D. Y.; Mei, X.; Ji, G.; Lu, M. H.; Xie, J. P.; Lu, J. M.; Lee, J. Y. *Angew. Chem. Int. Ed.* **2012**, *51*, 2409–2413.
- (25) Jia, H.; Gao, P.; Yang, J.; Wang, J.; Nuli, Y.; Yang, Z. *Adv. Energy Mater.* **2011**, *1*, 1036–1039.
- (26) Lee, J.-I.; Lee, K. T.; Cho, J.; Kim, J.; Choi, N.-S.; Park, S. *Angew. Chem. Int. Ed.* **2012**, *51*, 2767–2771.
- (27) Magasinski, A.; Dixon, P.; Hertzberg, B.; Kvit, A.; Ayala, J.; Yushin, G. *Nat. Mater.* **2010**, *9*, 353–358.
- (28) Zhou, W. C.; Upadhyay, S.; Whittingham, M. S. *Electrochim. Commun.* **2011**, *13*, 1102–1104.
- (29) Xu, Y.; Yin, G.; Cheng, X.; Zuo, P. *Electrochim. Acta* **2011**, *56*, 4403–4407.
- (30) Dong, H.; Ai, X. P.; Yang, H. X. *Electrochim. Commun.* **2003**, *5*, 952–957.
- (31) Li, T.; Cao, Y. L.; Ai, X. P.; Yang, H. X. *J. Power Sources* **2008**, *184*, 473–476.
- (32) Yoshio, M.; Wang, H.; Fukuda, K.; Umeno, T.; Dimov, N.; Ogumi, Z. *J. Electrochem. Soc.* **2002**, *149*, A1598–A1603.

(33) Obrovac, M. N.; Krause, L. J. *J. Electrochem. Soc.* **2007**, *154*, A103–A108.

(34) Li, H.; Huang, X. J.; Chen, L. Q.; Zhou, G. W.; Zhang, Z.; Yu, D. P.; Mo, Y. J.; Pei, N. *Solid State Ionics* **2000**, *135*, 181–191.

(35) Ghassemi, H.; Au, M.; Chen, N.; Heiden, P. A.; Yassar, R. S. *ACS Nano* **2011**, *5*, 7805–7811.

(36) Magasinski, A.; Zdyrko, B.; Kovalenko, I.; Hertzberg, B.; Burtovyy, R.; Huebner, C. F.; Fuller, T. F.; Luzinov, I.; Yushin, G. *ACS Appl. Mater. Interfaces* **2010**, *2*, 3004–3010.